Title:

Understanding the Electron-Doping Mechanism in Potassium-Intercalated Single-Walled Carbon Nanotubes

Author(s): Claudia Kröckel, María Rosa Preciado-Rivas, Victor Alexander Torres-Sánchez, Duncan J. Mow-bray, Stephanie Reich, Frank Hauke, Julio C. Chacón-Torres, and Andreas Hirsch

Citation:

"J. Am. Chem. Soc. 2020, 142, 5, 2327–2337
Publication Date:January 7, 2020
https://doi.org/10.1021/jacs.9b11370
Copyright © 2020 American Chemical Society"

Understanding the Electron-Doping Mechanism in Potassium-Intercalated Single-Walled Carbon Nanotubes

Claudia Kröckel,[†] María Rosa Preciado-Rivas,[‡] Victor Alexander Torres-Sánchez,[‡] Duncan J. Mowbray,[‡] Stephanie Reich,[§] Frank Hauke,[†] Julio C. Chacón-Torres,[*, ‡] and Andreas Hirsch[*, †]

[†]Department of Chemistry and Pharmacy and Joint Institute of Advanced Materials and Processes (ZMP), Friedrich-Alexander University of Erlangen-Nuremberg, Nikolaus-Fiebiger-Str. 10, 91058 Erlangen, Germany

[‡]Yachay Tech University, School of Physical Sciences and Nanotechnology, 100119-Urcuquí, Ecuador

[§]Department of Physics, Freie Universität Berlin, Arnimallee 14, 14195 Berlin, Germany

Supporting Information Placeholder

ABSTRACT: Single-walled carbon nanotubes (SWCNTs) can be doped with potassium, similar to graphite, leading to intercalation compounds. These binary systems exhibit a clear metallic character. However, the entire picture of how electron doping (*e*-doping) modifies the SWCNTs' vibrational spectra as a function of their diameter, chirality, and metallicity is still elusive. Herein, we present a detailed study of the intercalation and solid state reduction of metallic and semiconducting enriched HiPco® SWCNTs. We performed a combined experimental and theoretical study of the evolution of their Raman response with potassium exposure, focusing specifically on their radial breathing mode (RBM). We found the charge donated from the potassium atoms occupies anti-bonding π orbitals of the SWCNTs, weakening their C-C bonds, and reducing the RBM frequency. This RBM downshift with increasing doping level is quasi-linear with a step-like behavior when the Fermi level crosses a van Hove singularity for semiconducting species. Moreover, this weakening of the C-C bonds is greater with decreasing curvature, or increasing diameter. Overall, this suggests the RBM downshift with *e*-doping is proportional to both the SWCNT's integrated density of states (DOS) $\varrho(\varepsilon)$ and diameter d. We have provided a precise and complete description of the complex electron doping mechanism in SWCNTs up to a charge density of -18 me/C, far beyond that achievable by standard gate voltage studies, based on their excitation energy, diameter, band gap energy, chiral angle, and metallicity. This work is highly relevant to tuning the electronic properties of SWCNTs for applications in nanoelectronics, plasmonics, and thermoelectricity.

INTRODUCTION

Single-walled carbon nanotubes (SWCNTs) are considered to be one of the most promising materials in nanoelectronics, biomedicine and optics based on their outstanding optoelectronic properties.[1-4] These properties are mainly determined by their chiral angle θ and diameter d, which determine their metallic or semiconducting behavior.[5, 6]

The optical and vibronic properties in SWCNTs are defined by their so-called van Hove singularities (vHS), which are specific to each SWCNT chirality.[7, 8] Raman spectroscopy is the tool of choice to investigate these properties, focusing on individual SWCNT chiralities and diameters up to the bulk material. Depending on the selected excitation wavelength, only a few SWCNT species are in resonance, with each of them exhibiting a different Raman response observable through their radial breathing mode (RBM).[9] However, investigating the effects of charge transfer and doping in single-walled carbon nanotubes has been a challenge due to their multi-dispersive character with respect to their diameter, metallicity and chirality.

Previous investigations on the electron doping (*e*-doping) of SWCNT bundles revealed a diameter dependence of the doping process in a range between $0.9 \lesssim d \lesssim 1.2$ nm,[10] and laid out the influence of the *e*-doping behavior in SWCNT to the resonance conditions were a precise chirality assignment of the sample is indispensable.[11] These studies conducted in doped SWCNTs were focused mainly on explaining the evolution of the RBM intensity without considering in detail the RBM shift as a function of doping. In this case, the dependence of the RBM shift was only investigated for metallic SWCNTs[12] and not for a bulk standard sample of SWCNTs where semiconducting and metallic SWCNTs coexist. One way to approach the study of individual SWCNTs as a function of *e*-doping is using single-chirality enriched samples. There are methods already established to sort SWCNT bundles according to their metallicity[13-16] and chirality.[17, 18] Separation of HiPco® SWCNTs with respect to their metallicity is also feasible[19] exhibiting a wide, but specific distribution of SWCNTs chiralities and diameters.[10]

In this work, we present a systematic experimental and theoretical spectroscopic study of the low-frequency Raman vibrations observed in *e*-doped HiPco® SWCNTs. A precise deconvolution of the RBM region allowed us to assign every component to a specific chirality and to determine their diameter d. This assignment gave us the possibility to *in-situ* track the evolution of the metallic and semiconducting species present in our HiPco® SWCNTs by following the evolution of their RBM signal as a function of potassium (K) doping. Our experiments are in agreement with the trend observed for metallic SWCNTs, but also reveal a diameter dependent RBM shift of semiconducting species which was previously undescribed. Density functional theory (DFT) calculations confirmed our experimental findings

and showed the RBM frequencies in SWCNTs to be strongly dependent on the amount of charge transfer, which for instance depends on the carbon nanotubes' diameter, chirality, band gap energy, van Hove singularities, and corresponding electronic density of states (DOS). We provide for the first time a clear and precise description of the complex electron doping mechanism in SWCNTs based on their excitation energy, diameter, band gap energy, chiral angle and metallicity up to extremely high doping regimes. This work will be highly relevant in the scientific carbon community in tuning the electronic properties of SWCNTs for potential applications in nanoelectronics, plasmonics, and thermoelectricity.

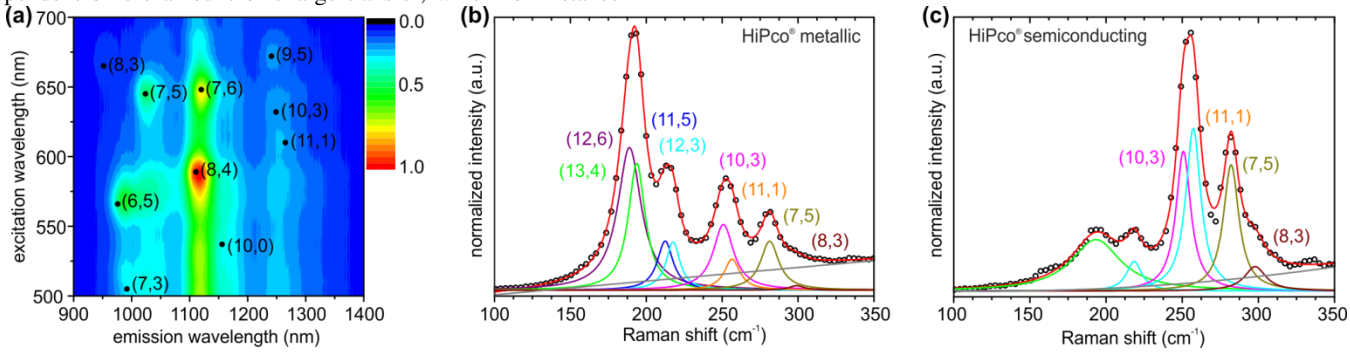

Figure 1. (a) Photoluminescence excitation map from HiPco® semiconducting pristine SWCNTs in SDBS, with chiralities marked by their (*n,m*) indices. Deconvolution of the RBM region measured at an excitation wavelength of 633 nm of the (b) metallic and (c) semiconducting enriched SWCNT sample with assigned chiralities.

RESULTS AND DISCUSSION

To determine the initial chirality distribution of the semiconducting enriched HiPco® SWCNTs we recorded a photoluminescence (PL) map of the pristine sample dispersed in an aqueous 1wt% sodium dodecylbenzene sulfonate (SDBS) solution (Figure 1(a)). Due to the quasi one-dimensional structure of SWCNTs, each species exhibits a defined set of optical transition energies E_{ii} depending on their diameter and chirality. When light is absorbed with a photon energy matching the E_{22} transition, a band-gap fluorescence can be obtained with an energy near the E_{11} transition. This brings the possibility to precisely determine the chiral indices (*n,m*) for each SWCNT present in a suspended bulk sample *via* fluorescence spectroscopy.[20] In Figure 1(a) we present the photoluminescence measurement of the semiconducting enriched pristine SWCNT sample dispersed in sodium dodecylbenzene sulfonate (SDBS) for excitation wavelengths in between 500 and 700 nm. The emission is plotted from 900 to 1400 nm.

We assigned the different species in our sample based on the empirical fitting model of the van Hove singularities of Weisman and Bachilo.[21] In our sample, we found a large variety of chiralities and diameters typical for HiPco® nanotubes.[22] The most prominent signals were located in an excitation region between 600 – 675 nm containing the (8,3), (8,4), (7,5), (7,6), (9,5), (10,3), and (11,1) chiralities. Additionally, the (6,5) chirality was present at an emission of ~ 985 nm. The slightly shifted emission signals compared to reference [21] can be explained by the different solvent used for preparing the SWCNT dispersion. In order to confirm our assignment, resonance Raman spectroscopy analyses were performed in the metallic and semiconducting enriched pristine SWCNT samples (Figure S1(a,b)). When examining the quality of both samples, they exhibited a low D/G-ratio value of around 0.076 for the metallic and 0.058 for the semiconducting sample indicating almost defect free pristine materials. In the RBM region of both samples four clear Raman bands were observed. The peaks in the 150 to 230 cm^{-1} can be attributed to the presence of metallic nanotubes, while in the region between 240 and 300 cm^{-1} semiconducting SWCNTs appeared when using an excitation wavelength of 633 nm.

In Figure 1(b,c), the deconvolution of the RBM peaks of the pristine metallic and semiconducting samples is shown, respectively. The RBM signals were fitted with Lorentzian functions. Our analysis confirmed the presence of the (8,3), (7,5), (10,3) and (11,1) chiralities previously observed by PL. Additional metallic chiralities were also found in the RBM region of Figure 1(b) and their complete assignment is presented in Table S1.

Having determined the SWCNT chiralities present in our sample, our next step was to monitor the *e*-doping of the enriched SWCNTs. For this purpose, a glass ampoule containing both K and a flake of the enriched HiPco® sample was sealed under high-vacuum conditions (~ 10^{-6} mbar) as depicted schematically in Figure 2(a). The glass ampoule was heated according to the two-zone vapor transport method, which has been confirmed to be effective when doping multi-walled[23] and single-walled[24] carbon nanotubes.

During this process, the K atoms donate their 4s electrons *via* a charge transfer mechanism to the SWCNTs that become negatively (*n-type*) doped species.[25] The evolution of the Raman spectrum of enriched HiPco® SWCNTs doped with K was recorded as a function of exposure time inside the sealed glass ampoule by conducting time dependent *in-situ* Raman spectroscopy. We used 633 nm as excitation wavelength since both metallic and semiconducting SWCNT species are in resonance at this energy. It is well known from the Raman spectrum in MWCNTs, that the G-line should evolve from a Lorentzian peak into a Fano-like one when highly *n-type* doping conditions exist.[23] After an exposure to K for about 48 and 60 minutes for the metallic and semiconducting sample, respectively, we reached a saturation level in the doped SWCNTs in which no further changes in the Raman spectrum were observable. This is shown in Figure 2(a,b) as the final doping level. The complete doping process was monitored for each sample in intervals of 1 min. Both samples showed a similar behavior while doping, as it can be seen from the evolution of the Raman spectra in Figure 2(a,b). The first conspicuous changes in the Raman spectra were noticed after 3 and 14 minutes in the metallic and semiconducting sample, respectively. For instance, the G-line in both samples turned into an asymmetric Fano-like shape characteristic for highly-doped SWCNT samples[26] with a lower frequency when compared to the pristine G-line peak. The RBM peaks vanished after about half an hour of doping in both cases. The disappearance of the 2D-line occurs also about 30 min after exposure to K. This behavior can be understood as the suppression of the double resonance process resulting from the highly doped conditions of the material. When trying to describe the evolution of the RBM spectrum as a function of doping, we found this process to be a much more complex mechanism to be analyzed requiring a precise and detailed deconvolution of the single peaks to understand their origin, shifts and intensity loss.

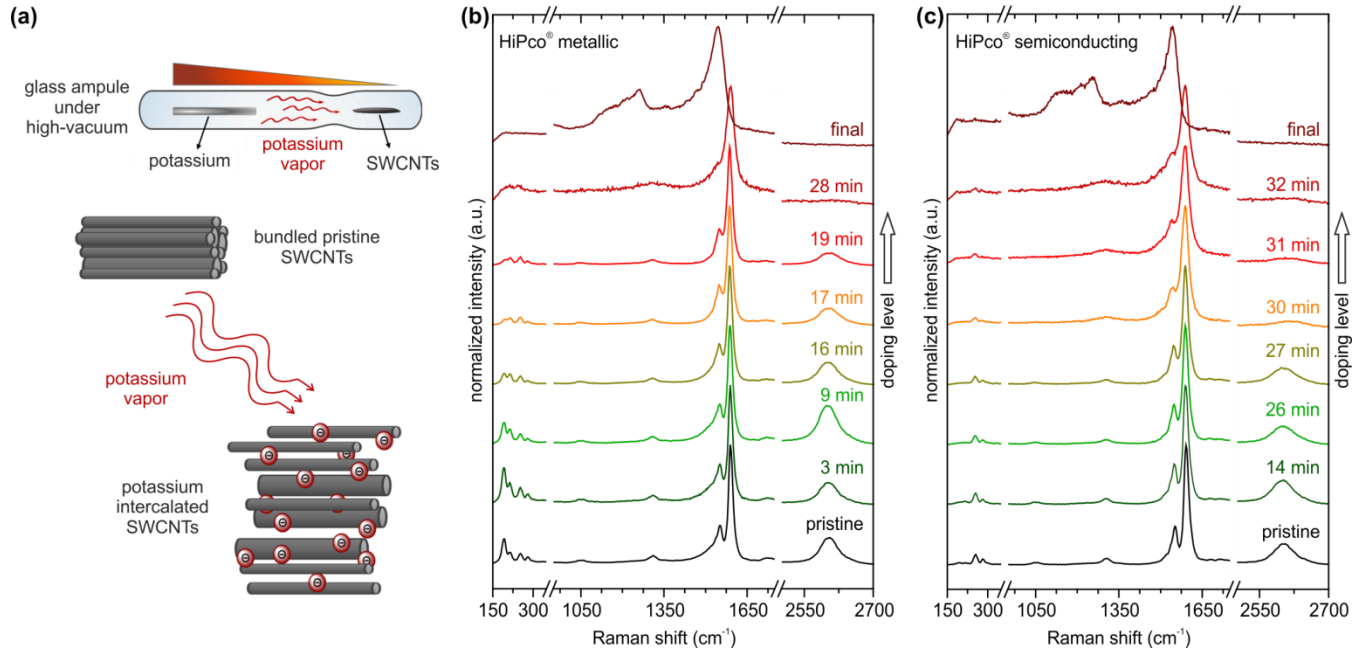

Figure 2. (a) Schematic of the SWCNT K doping process under high-vacuum conditions (~ 10^{-6} mbar). Evolution of the Raman spectra as a function of K doping at selected doping levels for the (b) metallic and (c) semiconducting enriched SWCNTs. The saturation level in the doped SWCNTs is marked as final doping level.

In Figure 3 we show the deconvolution of selected doping steps in the RBM spectra from the metallic and semiconducting SWCNT samples. At this point the intensity of every spectrum was normalized with respect to their G(+) peak. We observed first a slight enhancement of the RBM signal for metallic and semiconducting HiPco® SWCNTs after 3/9 and 14 minutes, respectively. Various explanations have been suggested for this behavior in the literature. We can now explain it as arising from a debundling of the bulk material due to a Coulomb repulsion caused by the additional negative charges within the samples.[27]

In the subsequent steps a continuous intensity loss as a function of K exposure time in the RBM region is noticeable (Figure S2). This effect has been reported before, especially for the RBM and G(-) vibrations, as being related to a shift of the Fermi energy level derived from a strong electron doping in SWCNTs.[28, 29] In this case, different van Hove singularities are filled upon the *e*-doping causing a change of the SWCNT resonance conditions.[29]

To understand the electron-doping mechanism in single-walled carbon nanotubes, the RBM signals were fitted with Lorentzian functions using a linear background for the metallic sample and a quadratic background for the semiconducting one due to the intense fluorescence resulting from the strong *n-type* doping in the material. We fitted the RBM signals in both samples until minutes 19 and 31, respectively, as the intensity afterwards was too low to obtain reliable fits. In the metallic sample we obtained four and three peaks in the RBM metallic and semiconducting regions, respectively, shown in Figure 3(a). For the semiconducting sample we found two and four peaks in the RBM metallic and semiconducting regions, respectively, shown in Figure 3(b).

To determine their corresponding specific chiralities, for each peak it is necessary to calculate their diameter from their corresponding Raman shift of the single peaks by using the equation:

$$\omega_{RBM} = \frac{\alpha}{d} + \omega_{0,} \qquad (1)$$

where ω_{RBM} is the measured RBM frequency, α describes the proportionality between RBM frequency and inverse diameter d in nm and ω_0 the interactions between SWCNTs in a bundle and with the substrate.[9, 30] We used α = 215x10^{-7} cm^{-1} and ω_0 = 18 cm^{-1} from reference [31]. These values were obtained from Kataura plot branches[31] and gave us an accurate description of our SWCNT species. In Table S1 we listed our fitted RBM frequencies, the calculated diameters, and the assigned chiralities. For comparison, we also added the theoretical diameters and the RBM frequency regions of the respective species.

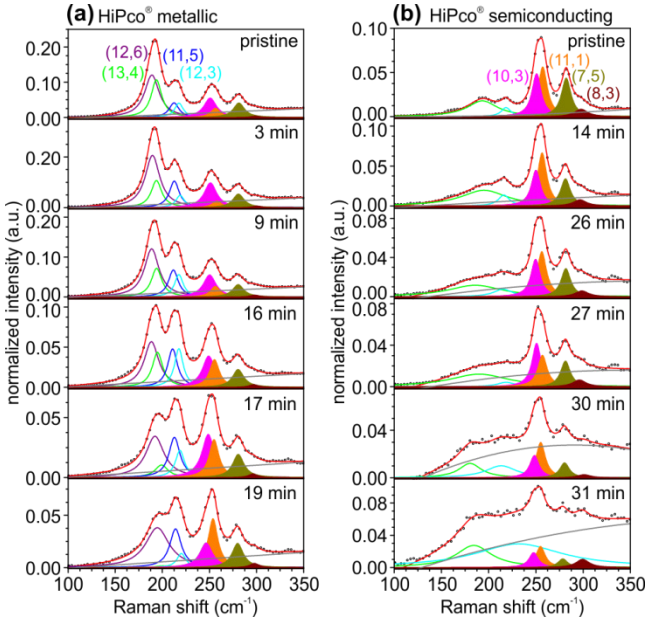

Figure 3. Deconvolution of the RBM signals from selected doping steps in the (a) metallic and (b) semiconducting enriched HiPco® SWCNT samples. Measured spectra (black open circles) and fitted signal (red line). SWCNTs peak assignment: (12,6) (violet), (13,4) (green), (11,5) blue, (12,3) (cyan), (10,3) (magenta), (11,1) (orange), (7,5) (dark yellow), and (8,3) (dark red). The filled peaks represent the semiconducting species and the open ones the metallic species.

For the peaks near 257 and 281 cm^{-1} two different chiralities could be assigned. The signal around 257 cm^{-1} could correspond to the (11,1) or (7,6) SWCNT, whereas the signal around

281 cm^{-1} belongs to either the (7,5) or (8,4). All of these species were also detected in the PL measurement (Figure 1(a)). However, Piao *et al.*[32] have measured the RBM Raman intensities in different single-enriched semiconducting SWCNT species, including these four chiralities. They found that (8,4) SWCNTs show nearly no RBM intensity signal and the (7,6) SWCNTs cause only a very weak signal at their corresponding resonance excitation wavelength. This is also in agreement with calculations from reference [33]. Based on these results, we were able to clearly assign these components to (11,1) and (7,5) SWCNTs in our samples.

Figure S2 shows the RBM frequency shift (a,b) and intensity evolution (c,d) from the (8,3), (7,5), (11,1) and (10,3) chiralities of the semiconducting species in the metallic and semiconducting sample, respectively, as a function of the K exposure time. In both samples the frequency of all investigated semiconducting chiralities, except for the (8,3), are downshifted when increasing the doping level. The (8,3) SWCNT underwent in the final analyzed step of the semiconducting sample a clear upshift. In the metallic sample we found that the smallest SWCNTs, (7,5) and (8,3), have the smallest downshift (~ 1.3 – 1.4 cm^{-1}) from pristine to the 19 min spectrum, followed by the (11,1) chirality with ~ 2.7 cm^{-1} downshift. The largest downshift was found for the (10,3) nanotube with about 4.3 cm^{-1}.

For the semiconducting sample the largest downshift was observed after 31 min for the (7,5) chirality with about 3.6 cm^{-1}, while the (8,3) SWCNT's RBM was upshifted by 1.5 cm^{-1}. The downshift of the (10,3) RBM was ~ 3.2 cm^{-1}. Also, the (11,1) nanotube exhibited a ~2.3 cm^{-1} lower frequency with respect to the undoped material. At this point, the (8,3) SWCNTs showed a very particular behavior. The lowest signal intensity and the smallest change in the intensity was obtained for the (8,3) SWCNT. The reason for this particular behavior could be attributable to the intrinsic resonance of this chirality. The resonance excitation wavelength for a (8,3) nanotube is located at ~ 665 nm according to both our PL measurements shown in Figure 1(a) and those of ref [21]. The energy difference between the (8,3) E_{22} resonance wavelength and our excitation wavelength for the Raman analysis (633 nm) is -0.089 eV. This means that the energy difference between the valence and conduction band of the second van Hove singularity is smaller than the applied excitation energy. This can already cause a large drop in the RBM Raman intensity as shown for other SWCNTs by resonance profiles[31, 32] and make the RBM of this species less sensitive to changes during the *n-type* doping.[29]

According to ref [21] and our PL measurement, the other three (7,5), (11,1) and (10,3) semiconducting chiralities are in a much better resonance when using a 633 nm excitation wavelength. There is no energy difference between E_{22} and our excitation wavelength for the (10,3) chirality, so this nanotube is perfectly in resonance. The energy difference of (7,5) is -0.037 eV and of (11,1) +0.07 eV. The intensities of all three chiralities behaved nearly the same with doping. In both samples first an increase in the intensity at the beginning of the doping was obtained. As the doping level increased, the intensities decreased caused by the shift of the Fermi level. During this analysis, only the (11,1) chirality did not follow this trend in the metallic enriched sample.

At the beginning of the doping process, the metallic SWCNTs showed a similar behavior as the semiconducting species, that is, a downshift in their RBM frequency (Figure S3). However, after 16 min of K exposure every metallic species underwent an upshift in their RBM signal. In particular, for the (13,4) chirality a slight upshift could be obtained already starting after 4 min. We found an overall upshift to be more prominent for the larger diameter chiralities, with ~ 5.8 cm^{-1} for the (12,6) and ~ 6.7 cm^{-1} for the (13,4) ones. For the smaller diameter (11,5) and (12,3) SWCNTs the upshift was of about 1.6 cm^{-1} and 2.6 cm^{-1}, respectively. It is important to note that the upshift was accompanied by a peak broadening which was most prominent for the (12,6) and (13,4) chiralities after 19 min with an increase of the full-width-at-half-maximum (FWHM) of about 12 cm^{-1} and 6 cm^{-1} compared to pristine, respectively. Furthermore, we found that the metallic species underwent a faster RBM intensity loss in comparison to the semiconducting species. This indicates a faster doping, especially in larger diameter metallic SWCNTs, since the intensity loss was more pronounced for the (13,4) and (12,6) chiralities. The downshift we observed in our SWCNT samples with respect to the doping level was also found by Öberg *et al.*[34] at the DFT level. They proposed different factors influencing the RBM shift depending on the functionalization of a (6,6) metallic SWCNT. One of these factors involved the charge transfer effect from either a functional group or the surrounding to the SWCNT. With increasingly negative charges the Fermi level experiences an upshift, which they found leading to a linear increase in the C-C bond length.[34] This is accompanied by an increase in the SWCNT's diameter[25] d, resulting in a downshift of the RBM frequency. Another factor is a decrease in the van Hove spacing causing a red-shift of the resonance energy.[34] The latter effect explains the decrease in the signal intensity of the RBMs with increasing doping level and supports our interpretation of the resonance loss of the metallic species.

In order to obtain an overall picture of the RBM development observed and to be sure of the general trend of the frequency changes as a function of the electron uptake the experimental results were cross checked and compared to *ab-initio* calculations. We conducted DFT calculations of the vibrational modes for negatively charged (8,4) and (10,0) semiconducting SWCNTs, which were both seen in our PL measurements in Figure 1(a). In this way we could investigate the effect of *e*-doping on the RBM frequency shift for semiconducting SWCNTs in comparison to the metallic (6,6) species as studied in reference [34], with both sets of SWCNTs having similar diameters of d ~ 0.8 nm. The calculated RBM vibrational frequencies for the undoped (8,4) and (10,0) SWCNTs were 263 and 304 cm^{-1}, respectively. This is in a reasonable agreement with the vibrational modes of 270 and 286 cm^{-1} that we obtained from Eq. (1) when using $\alpha = 224 \times 10^{-7}$ and $\omega_0 = 0$ from ref [35] for isolated SWCNTs.

The RBM frequency shifts $\Delta\omega_{RBM}(q)$ of the negatively doped species were modeled by shifting up the Fermi level to the SWCNTs self-consistently to have the required charge q. In Figure 4(a,b) we show the calculated change in the RBM frequency of the (8,4) and (10,0) SWCNTs with their charge in millielectrons per C atom (me/C). In agreement with Öberg *et al.* for metallic (6,6) SWCNTs,[34] we observed a linear downshift in the RBM frequency with increasing the doping level. Surprisingly, this downshift revealed a step-like structure in semiconducting species.

In order to compare the influence of the *e*-doping in metallic and semiconducting species we first consider the negative charge $\Delta\rho$ necessary to cause an RBM frequency downshift of 1 cm^{-1}. For the (8,4) and (10,0) SWCNTs we obtained $\Delta\rho$ ~ -2.6 and -2.9 me/C, respectively, an order of magnitude less than the $\Delta\rho$ ~ -22.1 me/C required for the (6,6) SWCNT.[34] This suggests that providing sufficient charge to fill the first van Hove singularity is sufficient to downshift the RBM, and the required charge is an order of magnitude higher for metallic compared to semiconducting SWCNTs, when they are isolated. Of course in a mixed sample, metallic tubes would be charged first before semiconducting tubes, as we will discuss.

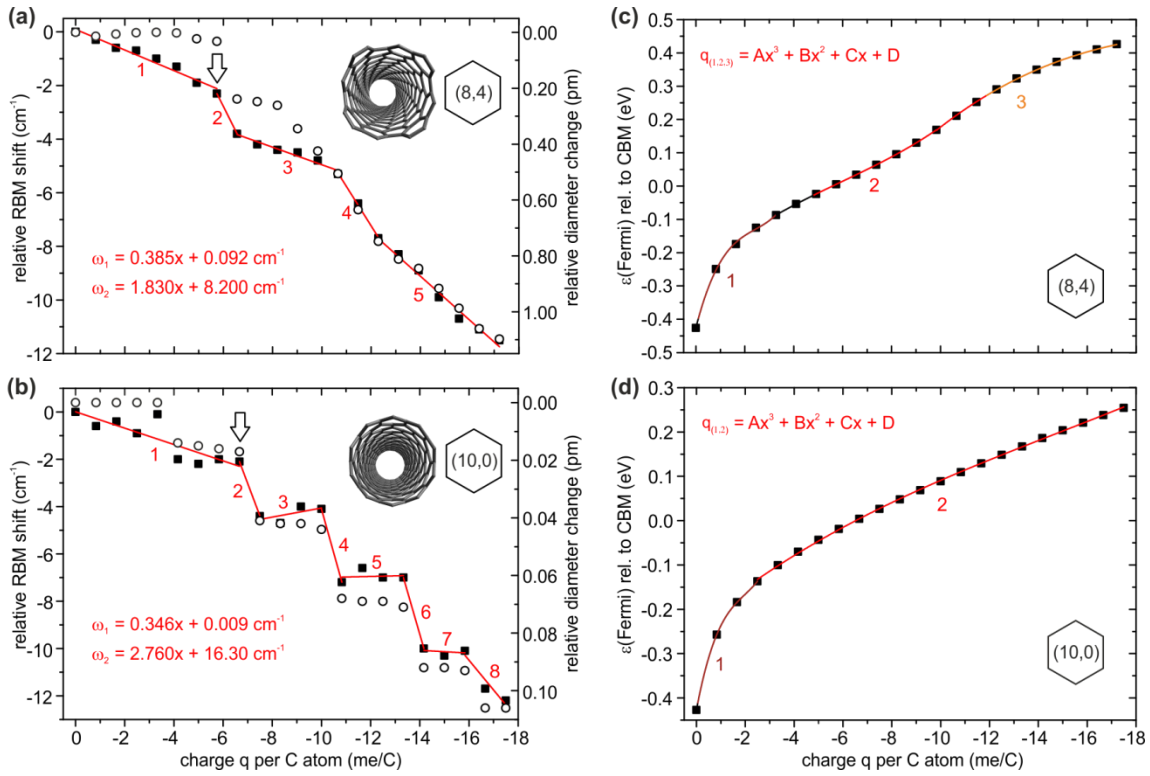

Figure 4. DFT calculated (a,b) RBM frequency shift in cm^{-1} (filled squares), change of the SWCNT diameter *d* in pm (open circles), and (c,d) Fermi energy ε_F relative to the conduction band minimum (CBM) in eV *versus* the charge *q* in millielectrons per C atom (me/C) for (a,c) (8,4) and (b,d) (10,0) SWCNTs. Fits to the frequency change are provided in red. At negative charges greater than (c) -5.6 and (d) -6.5 me/C the Fermi energy reaches the first van Hove singularity.

In Figure 4 (a,b) we also show the calculated change in the (8,4) and (10,0) SWCNTs' diameters *d* with charge, which closely follows the step-like behavior of the RBM. An elongation of the C-C bond by about 0.25 pm or 17% in the (6,6) SWCNT was obtained by Öberg et. al at a charge of -16.7 me/C.[34] However, our calculations of *e*-doped (8,4) and (10,0) semiconducting SWCNTs showed the diameter *d* hardly changed for a similar doping level. Contrary to Öberg et. al, the C-C bond length of the (10,0) SWCNT seem to be less affected by the electron uptake with respect to the (6,6) SWCNT[36] which is more in agreement to our findings and suggest that the observed downshift of the RBM in semiconducting SWCNTs may be influenced by parallel factors that will define the origin of their RBM shift.

Rather than the structural change itself, we will now consider how the electronic structure of the *e*-doped SWCNT may cause the observed downshift of the RBM frequency, $\Delta\omega_{RBM}(q)$. Figures 4(c) and (d) show the charge required for the Fermi level ε_F to cross the conduction band minimum (CBM), *i.e.*, the first van Hove singularity, for the (8,4) and (10,0) of -5.6 and -6.5 me/C, respectively. It is very remarkable to see that these same amount of electron uptake is required to obtain a step/jump in both the RBM shift and diameter for each tube (region 2 in Figure 4(a,b)). This suggest that: i) regions, with gentler slopes, *e.g.* region 1 and 3 of Figure 4(a,b) represent the transition where the Fermi energy level is shifting into a van Hove singularity; and ii) sections with steeper slopes, *e.g.* regions 2 and 4 of Figure 4(a) and (b) represent the moment in which the Fermi level coincides with a van Hove singularity.

When the Fermi level coincides with a van Hove singularity, i.e., $\varepsilon_F \approx \varepsilon_{vHS}$, the donated charge is occupying many anti-bonding π orbitals of the *e*-doped SWCNT. This leads to an elongation and weakening of the C-C bonds, reducing the energy required to radially expand the SWCNT, *i.e.*, downshifting the RBM frequency. Moreover, we found this weakening of the C-C bonds is reduced with increasing curvature, or decreasing the diameter *d*. This suggests the change in the RBM shift $\Delta\omega_{RBM}$ with *e*-doping to be proportional to both the SWCNT's density of states (DOS) $\varrho(\varepsilon)$ and the diameter *d*, so that:

$$\Delta\omega_{RBM}(q) \approx -Cd\int_{\varepsilon_F(0)}^{\varepsilon_F(q)} \varrho(\varepsilon)d\varepsilon, \qquad (2)$$

where $\varepsilon_F(q)$ and $\varepsilon_F(0)$ are the Fermi levels of the *e*-doped and neutral SWCNTs, respectively, and *C* is a constant of proportionality. The negative sign in Eq. (2) reflects the observed downshifting of the RBM as anti-bonding states being occupied.

Away from the van Hove singularities, the SWCNT's DOS is relatively constant, thus Eq. (2) simplifies to $\Delta\omega_{RBM}(q) \sim Cqd$. By comparing the fits to $\Delta\omega_{RBM}$ for $\varepsilon_F \lesssim \varepsilon_{CBM}$ in Figures 4(a) and b), we observed the larger diameter (8,4) SWCNT indeed has a steeper slope ($\alpha \approx 0.385$ cm^{-1} $(me/C)^{-1}$; $d \approx 0.840$ nm) than the smaller diameter (10,0) SWCNT ($\alpha \approx 0.346$ cm^{-1} $(me/C)^{-1}$; d ≈ 0.792 nm), consistent with a linear dependence on the SWCNT's diameter *d*. These results would then yield an RBM downshift of

$$\Delta\omega_{RBM}(q) \sim 0.8qd \text{ for } \varepsilon_F \lesssim \varepsilon_{CBM} \qquad (3)$$

where *q* is in me/C and *d* is in nm.

To test the validity of this model empirically, we compared it to the measured RBM shifts for four different *e*-doped semiconducting SWCNTs present in the semiconducting and metallic enriched sample, as shown in Figure 5. In each case we see the RBM initially undergoes a linear downshift prior to a sharper drop after 800 to 1000 Langmuir of K exposures, marked by arrows in Figure 5(a). This dramatic decrease in the RBM frequency is consistent with the filling of the *e*-doped SWCNT's CBM, *i.e.*, the first van Hove singularity. Moreover, the initial slope exhibits a quasi-linear dependence on the diameter, with $d \approx 0.784$, 0.831, 0.916, and 0.936 nm for the (8,3), (7,5), (11,1) and (10,3) SWCNTs, respectively[37] (Figure 5 (b,c)). These findings provide empirical justification of our model of the RBM downshift provided in Equations (2) and (3).

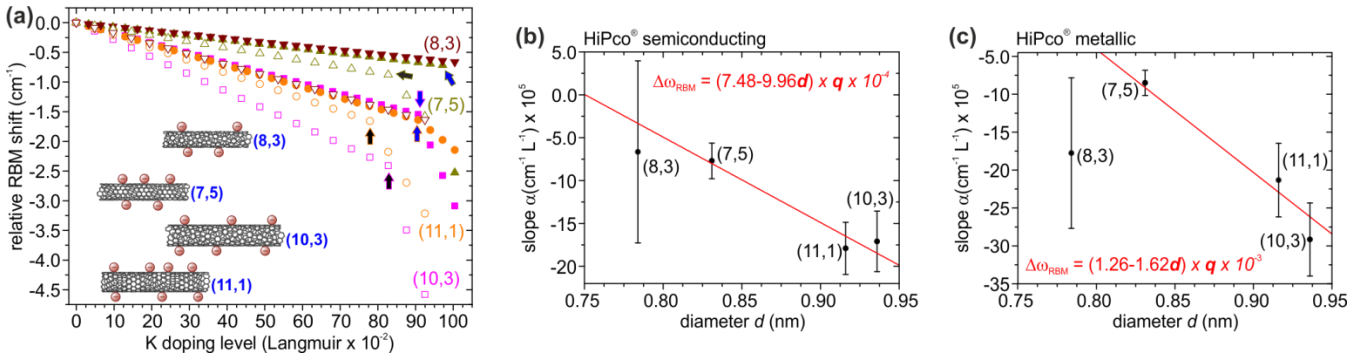

Figure 5. (a) Fitted RBM shifts of the semiconducting SWCNTs (λ_{exc} = 633 nm) with increasing K doping level in Langmuir in the metallic (open symbols) and semiconducting (filled symbols) enriched samples. Arrows indicate the observed shift of the Fermi energy (ε_F) into the first van Hove singularity of the respective species in the metallic (black) and semiconducting (blue) sample. Linear fits of the slope α (obtained from Figure S4) *versus* the SWCNT diameter for the (b) semiconducting and (c) metallic sample and given relation of the RBM frequency downshift $\Delta\omega_{RBM}$ with the diameter d and the potassium exposure time q.

The *e*-doped semiconducting SWCNTs generally follow the same trend in the metallic and semiconducting samples, with the larger diameter species being more affected by doping, as seen from the larger downshift. In the semiconducting sample the larger diameter (10,3) and (11,1) SWCNTs underwent a more pronounced RBM downshift with K exposure compared to the smaller diameter (7,5) and (8,3) chiralities. Within the same diameter range there were only small deviations of the RBM shift. We find a step in the RBM downshift occurring for K exposures of 9100 Langmuir for (11,1) and (10,3) and 9700 Langmuir for the (7,5) SWCNTs, being this one the largest.

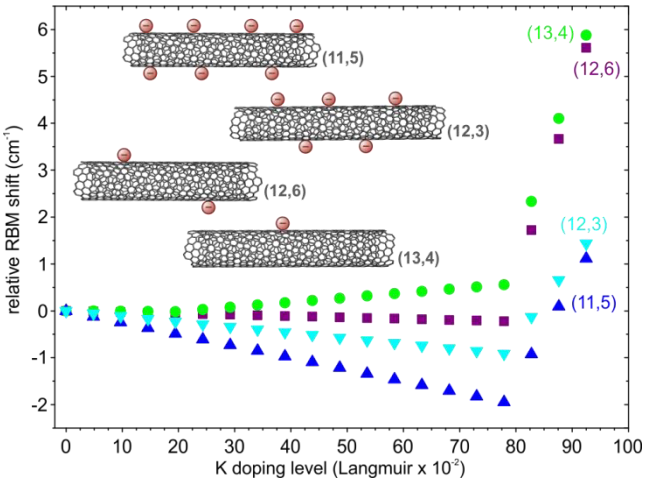

Figure 6. Measured RBM shifts of the metallic SWCNTs (λ_{exc} = 633 nm) with increasing K doping level in Langmuir in the metallic enriched sample. The amount of electrons on the respective SWCNTs indicates the influence of the charges on the observed downshift.

Turning into the analysis of the metallic enriched sample, we find the RBM downshift proceeds faster than in the semiconducting enriched sample, especially for the (10,3) and (8,3) SWCNTs. This may be related to intertube interactions between metallic and semiconducting SWCNTs during the *e*-doping.[38] The step in the RBM downshift was obtained at 7790 Langmuir for (11,1) and 8280 Langmuir for (10,3) and (7,5) SWCNTs (Figure 5(a)). We find the step appears at lower K exposures in the metallic nanotubes when compared to the semiconducting species. This may be related to a larger charge donation from K to the SWCNTs in mixed metallic/semiconducting samples,[38] resulting in a greater shift of the Fermi energy for similar K exposures.

Similar to semiconducting SWCNTs, all *e*-doped metallic SWCNTs also show a downshift in their RBM frequency with increasing the doping level, as shown in Figure 6. However, in contrast to the semiconducting species, this trend is followed by a sharp upshift at a certain K exposure. We find the downshift to be more pronounced for (11,5) followed by (12,3) and (12,6). The weakest downshift was found for (13,4), and already changed into an upshift after 4 minutes of K exposure. The slope of the upshift was largest for (12,6) followed by (13,4), (11,5) and (12,3). However, to get a comparable value for the upshift, the preceding downshift has to be considered, so it is more appropriate to compare the overall shift with the RBM shift of the pristine material. In this case (13,4) is most upshifted followed by (12,6), (12,3) and (11,5). The upshift which we have observed for *e*-doped metallic SWCNTs is similar to that described by Farhat *et al.* for individual metallic SWCNTs in small bundles.[12] They reported an RBM upshift of ~ 2 cm^{-1} when applying a gate voltage.[12] The larger overall upshifts in the RBM frequency in comparison to ref [12] may be attributed to the higher doping level we achieved by K doping. The increase in the FWHM in our sample, which was not obtained in that extend in ref [12], could be explained by a strong electron phonon coupling (*e-ph*) in the highly *e*-doped sample.[39]

Farhat et al. suggested the observed upshift in the RBM frequency may be due to an electron-phonon coupling process specific for metallic SWCNTs.[12] This coupling could be influenced by the Fermi energy level shift relative to the Dirac point, resulting in the observation of the "bare" RBM phonon frequencies and they found this process more pronounced for small-diameter and small chiral angle metallic species.[12] This observation is also reflected in the downshift obtained in our measurements which disclosed two main trends:

(i) Within the diameter range of the metallic species observed with a 633 nm excitation wavelength the larger-diameter SWCNTs show a less pronounced downshift, *i.e.*, the (11,5) and (12,3) chirality belong to the $2n + m = 27$ family whereas (12,6) and (13,4) belong to the $2n + m = 30$ family. The lower the family number the more pronounced was the obtained RBM frequency downshift. The lower the families' number the lower also the average diameter of the SWCNTs of the respective family. This suggests that in smaller diameter metallic *e*-doped SWCNTs the influence of the charges on the C-C bond length is stronger and thus the downshift becomes more significant.

(ii) Within a family the chiral angle determines the downshift which is more pronounced for small chiral angles. Considering for example the 27 family with (11,5) (θ = 17.8°) and (12,3) (θ = 10.9°) then a larger RBM frequency downshift is obtained for (11,5) with the larger chiral angle but smaller diameter (1.111 nm compared to (12,3) with 1.076 nm). This trend is consistent with the results from Farhat *et al.* for the $2n + m = 24$ family.[12]

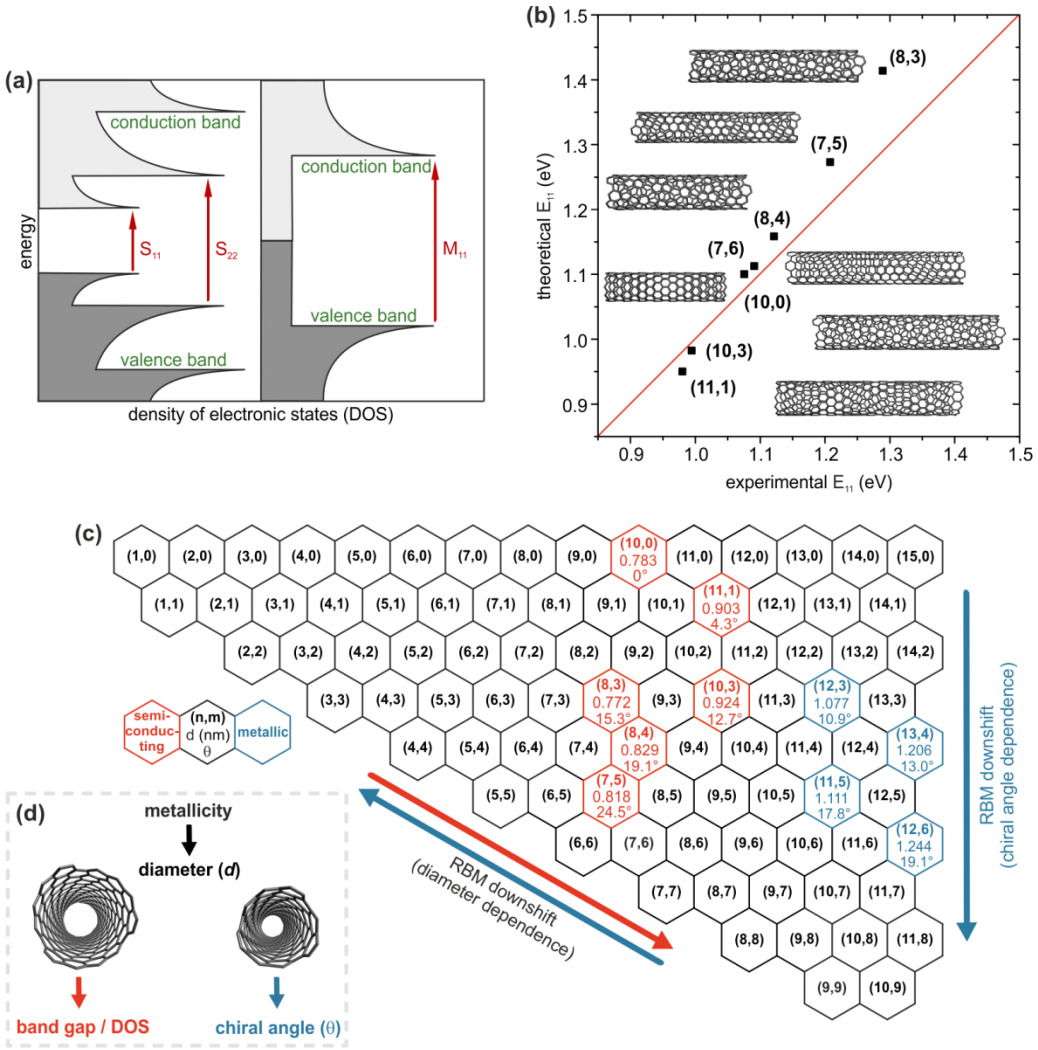

Figure 7. (a) Schematic of the electronic density of states of semiconducting (left) and metallic (right) SWCNTs, with optical transitions between the first (S_{11}/M_{11}) and second (S_{22}) van Hove singularity marked in red. (b) Theoretical versus experimental E_{11} transition energies for the semiconducting HiPco® SWCNT samples from refs [37] and [40], respectively. (c) SWCNT indices (n,m) with semiconducting (red) and metallic (blue) SWCNTs in our samples marked. Diameter d and chiral angle θ dependence of the e-doping process and RBM downshift marked by arrows. (d) Schematic of the main factors influencing the e-doping in SWCNTs.

CONCLUSIONS

Our overall results are summarized in Figure 7. We have shown that providing enough charge to fill the first van Hove singularity in either metallic (M_{11}) or semiconducting SWCNTs (S_{11}) (Figure 7(a)) is sufficient to downshift their corresponding RBM frequency. Moreover, the required charge is an order of magnitude higher for metallic compared to semiconducting SWCNTs. When the Fermi energy level coincides with a van Hove singularity, *i.e.*, $\varepsilon_F \approx \varepsilon_{vHS}$, the donated charge is occupying many anti-bonding π orbitals of the e-doped SWCNT. This leads to a weakening of the C-C bonds, reducing the energy required to radially expand the SWCNT, and downshifting their RBM frequency. In semiconducting SWCNTs we found this weakening of the C-C bonds to be reduced when increasing the curvature, or decreasing the diameter d. In addition, for similar diameters it is ruled by the band gap energy E_{11}. Figure 7(b) illustrates the theoretical *versus* experimental E_{11} transition energies from refs [37] and [39] for the semiconducting SWCNT species found in our enriched HiPco® samples.

We revealed for the first time a generic trend in the e-doping behavior of SWCNTs as depicted in Figures 7(c) and (d) and summarize as follows:

(i) Metallic SWCNTs are e-doped first, as deduced from their immediate RBM shift and intensity loss. In contrast to the semiconducting species, the electron uptake in metallic SWCNTs is affected in addition to the diameter d also by their chiral angle θ. Their final RBM frequency shift can be assumed from the combination of the C-C bond weakening and the e-ph coupling effect described in ref [12].

(ii) For semiconducting SWCNTs, using a combined experimental and theoretical approach, we were able to confirm that the RBM downshift is directly proportional to the SWCNT's diameter d, and the integrated DOS occupied with additional electrons. This leads to an RBM downshift with a step-like behavior, where the steps are at charging levels at which the Fermi energy level ε_F and a van Hove singularity in the DOS ε_{vHS} coincide.

(iii) When having both metallic and semiconducting SWCNTs, the RBM shift with e-doping will depend directly on both their diameter d and their electronic density of states (DOS). These parameters will rule the order in which each carbon nanotube will be doped.

We have provided a novel metrology to describe the complex electron doping mechanism in SWCNTs, pointing the order in which electrons will charge the diverse carbon nanotubes present in the sample based on their excitation energy, diameter, band gap energy, chiral angle, and metallicity. This work will serve as a

roadmap to fine tune the electronic properties of SWCNTs for future applications in nanoelectronics, plasmonics, and thermoelectricity.

EXPERIMENTAL SECTION

Experimental Design. The electronically enriched HiPco® SWCNT materials (NanoGauge IsoTubes semiconducting enriched SWCNTs >98% and >95% metallic enriched SWCNTs) were purchased from NanoIntegris Technologies Inc., Canada. The pristine SWCNTs were pre-cleaned by heating them at 150 °C overnight in a glove box under an argon atmosphere (O_2 < 0.1 ppm, H_2O < 0.1 ppm) and were additionally cleaned under high-vacuum conditions (~ 10^{-6} mbar) at ~ 400 °C . The *in-situ* Raman analyses of metallic and semiconducting SWCNTs were done in a glass ampule sealed together with potassium (99.95% purity, Sigma Aldrich) under high-vacuum conditions (~10^{-6} mbar). The progress of the doping was monitored with a Witec alpha300 RA Raman spectrometer at 633 nm excitation wavelength while evaporating the potassium at ~ 90 °C. The spectra were recorded every minute until a full intercalation was achieved. The fluorescence map analysis was acquired from the HiPco® semiconducting sample dispersed in an aqueous SDBS solution (1wt%) with a Horiba Fluorolog iHR320 equipped a liquid nitrogen cooled IGA detector.

Computational Details. All DFT calculations employed the GPAW code[41, 42] within the atomic simulation environment.[43, 44] We employed the local density approximation[45] for the exchange and correlation (xc) functional, a grid spacing of h ≈ 0.2 Å, 3 k-points along the SWCNT's axis, and an electronic broadening of kBT = 0.1 eV with all energies extrapolated to T → 0. The Kohn-Sham wavefunctions were represented using linear combinations of atomic orbitals (LCAOs)[46] with double-ζ-polarized (DZP) basis sets. We used a single unit cell of 112 atoms for the (8,4) SWCNT (L ≈ 1.134 nm) and a threefold unit cell for the (10,0) SWCNT (L ≈ 1.289 nm) containing 120 atoms, with more than 10 Å of vacuum perpendicular to the SWCNT's axis. The repetition of the (10,0) SWCNT's unit cell along its axis was necessary to include both in and out of phase radial breathing modes. Both the fully periodic unit cells and atomic structures were relaxed until a maximum force less than 0.05 eV/Å was obtained for each charge q. The charge transfer to the SWCNT from the K atoms was modeled self-consistently as a fixed upward shift of the Fermi level, which has previously proven successful in describing K doped SWCNTs.[47] Vibrational modes were obtained applying a displacement of $\Delta \approx 0.1$ Å for each atom in each direction to the relaxed structure to obtain the dynamical or hessian matrix for the charged SWCNTs.

Each section of the step-like $\Delta\omega_{RBM}(q)$ curve was modeled by individual linear fits with different slopes, leading to 5 different sections for the (8,4) and 8 sections for the (10,0) chirality depicted as red lines in Figure 4(a,b). The functions for the first sections for (8,4) and (10,0) are given by the equation $\omega 1 = 0.385x + 0.092$ cm^{-1} and $\omega 1 = 0.346x + 0.009$ cm^{-1}, respectively. The slope of the linear functions describes the influence of *e*-doping on the RBM frequency shift.

ASSOCIATED CONTENT

Supporting Information

The Supporting Information is available free of charge on the ACS Publications website at DOI: 10.1021/jacs.xxxxxxx.

RBM fitting procedure; Pristine spectra of the metallic and semiconducting enriched HiPco® SWCNTs; Calculated chiralities; RBM shift and intensity development of the semiconducting SWCNTs; RBM shift and intensity development of the metallic SWCNTs in the metallic sample; Linear fitting functions of the calculated RBM frequency downshift for the (8,4) SWCNT; Linear fitting functions of the calculated RBM frequency downshift for the (10,0) SWCNT; Parameters of the cubic spline fit for the (8,4) SWCNT relative Fermi shift to the CBM; Parameters of the cubic spline fit for the (10,0) SWCNT relative Fermi shift to the CBM; Linear fittings of the RBM frequency downshifts in the semiconducting species; Linear fittings of the RBM frequency downshifts in the metallic species; Calculation of the free energy ΔF^0 and pressure of the potassium vapor phase in our samples (PDF)

AUTHOR INFORMATION

Corresponding Authors

*E-mail: jchacon@yachaytech.edu.ec.

*E-mail: andreas.hirsch@fau.de.

Notes

The authors declare no competing financial interests.

ACKNOWLEDGMENTS

The authors acknowledge the financial support of the Deutsche Forschungsgemeinschaft (DFG-SFB 953; Project A1 "Synthetic Carbon Allotropes"). This work used the Imbabura cluster of Yachay Tech University, which was purchased under contract No. 2017-024 (SIE-UITEY-007-2017). J. Chacón-Torres and S. Reich thank the DRS Postdoc Fellowship Point-2014 of the NanoScale Focus Area at Freie Universität Berlin for financial support.

REFERENCES

(1) Avouris, P.; Freitag, M.; Perebeinos, V., Carbon-nanotube photonics and optoelectronics. *Nat. Photonics* **2008**, *2*, 341-350.

(2) Avouris, P.; Chen, Z.; Perebeinos, V., Carbon-based electronics. *Nat. Nanotechnol.* **2007**, *2*, 605-615.

(3) Farrera, C.; Torres Andon, F.; Feliu, N., Carbon Nanotubes as Optical Sensors in Biomedicine. *ACS Nano* **2017**, *11*, 10637-10643.

(4) Cherukuri, P.; Bachilo, S. M.; Litovsky, S. H.; Weisman, R. B., Near-infrared fluorescence microscopy of single-walled carbon nanotubes in phagocytic cells. *J. Am. Chem. Soc.* **2004**, *126*, 15638-15639.

(5) Odom, T. W.; Huang, J.-L.; Kim, P.; Lieber, C. M., Atomic structure and electronic properties of single-walled carbon nanotubes. *Nature* **1998**, *391*, 62-64.

(6) Reich, S.; Thomsen, C.; Maultzsch, J., *Carbon Nanotubes: Basic Concepts and Physical Properties*. Wiley-VCH Verlag GmbH & Co. KGaA: Weinheim, Germany, **2004**.

(7) Jorio, A.; Souza Filho, A. G.; Dresselhaus, G.; Dresselhaus, M. S.; Saito, R.; Hafner, J. H.; Lieber, C. M.; Matinaga, F. M.; Dantas, M. S. S.; Pimenta, M. A., Joint density of electronic states for one isolated single-wall carbon nanotube studied by resonant Raman scattering. *Phys. Rev. B* **2001**, *63*, 245416.

(8) Kramberger, C.; Rauf, H.; Shiozawa, H.; Knupfer, M.; Büchner, B.; Pichler, T.; Batchelor, D.; Kataura, H., Unraveling van Hove singularities in x-ray absorption response of single-wall carbon nanotubes. *Phys. Rev. B* **2007**, *75*, 235437.

(9) Kuzmany, H.; Plank, W.; Hulman, M.; Kramberger, C.; Grüneis, A.; Pichler, T.; Peterlik, H.; Kataura, H.; Achiba, Y., Determination of SWCNT diameters from the Raman response of the radial breathing mode. *Eur. Phys. J. B* **2001**, *22*, 307-320.

(10) Kukovecz, A.; Pichler, T.; Pfeiffer, R.; Kramberger, C.; Kuzmany, H., Diameter selective doping of single wall carbon nanotubes. *Phys. Chem. Chem. Phys.* **2003**, *5*, 582-587.

(11) Kavan, L.; Kalbáč, M.; Zukalová, M.; Dunsch, L., Electrochemical Doping of Chirality-Resolved Carbon Nanotubes. *J. Phys. Chem. B* **2005**, *109*, 19613-19619.

(12) Farhat, H.; Sasaki, K.; Kalbac, M.; Hofmann, M.; Saito, R.; Dresselhaus, M. S.; Kong, J., Softening of the radial breathing mode in metallic carbon nanotubes. *Phys. Rev. Lett.* **2009**, *102*, 126804-126804.

(13) Green, A. A.; Hersam, M. C., Ultracentrifugation of single-walled nanotubes. *Mater. Today* **2007**, *10*, 59-60.

(14) Liu, H.; Nishide, D.; Tanaka, T.; Kataura, H., Large-scale single-chirality separation of single-wall carbon nanotubes by simple gel chromatography. *Nat. Commun.* **2011**, *2*, 1313/1-1313/8.

(15) Green, A. A.; Hersam, M. C., Colored Semitransparent Conductive Coatings Consisting of Monodisperse Metallic Single-Walled Carbon Nanotubes. *Nano Lett.* **2008**, *8*, 1417-1422.
(16) Reis, W. G.; Tomović, Ž.; Weitz, R. T.; Krupke, R.; Mikhael, J., Wide dynamic range enrichment method of semiconducting single-walled carbon nanotubes with weak field centrifugation. *Sci. Rep.* **2017**, *7*, 44812.
(17) Graf, A.; Zakharko, Y.; Schießl, S. P.; Backes, C.; Pfohl, M.; Flavel, B. S.; Zaumseil, J., Large scale, selective dispersion of long single-walled carbon nanotubes with high photoluminescence quantum yield by shear force mixing. *Carbon* **2016**, *105*, 593-599.
(18) Ghosh, S.; Bachilo, S. M.; Weisman, R. B., Advanced sorting of single-walled carbon nanotubes by nonlinear density-gradient ultracentrifugation. *Nat. Nanotechnol.* **2010**, *5*, 443 - 450.
(19) Yanagi, K.; Miyata, Y.; Kataura, H., Optical and Conductive Characteristics of Metallic Single-Wall Carbon Nanotubes with Three Basic Colors; Cyan, Magenta, and Yellow. *Appl. Phys. Express* **2008**, *1*, 034003.
(20) Bachilo, S. M.; Strano, M. S.; Kittrell, C.; Hauge, R. H.; Smalley, R. E.; Weisman, R. B., Structure-Assigned Optical Spectra of Single-Walled Carbon Nanotubes. *Science* **2002**, *298*, 2361 - 2366.
(21) Weisman, R. B.; Bachilo, S. M., Dependence of Optical Transition Energies on Structure for Single-Walled Carbon Nanotubes in Aqueous Suspension: An Empirical Kataura Plot. *Nano Lett.* **2003**, *3*, 1235-1238.
(22) Tyborski, C.; Herziger, F.; Maultzsch, J., Raman spectroscopy of nondispersive intermediate frequency modes and their overtones in carbon nanotubes. *Phys. Status Solidi B* **2015**, *252*, 2551-2557.
(23) Chacón-Torres, J. C.; Dzsaber, S.; Vega-Diaz, S. M.; Akbarzadeh, J.; Peterlik, H.; Kotakoski, J.; Argentero, G.; Meyer, J. C.; Pichler, T.; Simon, F., et al., Potassium intercalated multiwalled carbon nanotubes. *Carbon* **2016**, *105*, 90-95.
(24) Pichler, T.; Sing, M.; Knupfer, M.; Golden, M. S.; Fink, J., Potassium intercalated bundles of single-wall carbon nanotubes: electronic structure and optical properties. *Solid State Commun.* **1999**, *109*, 721-726.
(25) Hansson, A.; Stafström, S., Electronic structure calculations of potassium-intercalated single-walled carbon nanotubes. *Phys. Rev. B* **2005**, *72*, 125420.
(26) Rao, A. M.; Eklund, P. C.; Bandow, S.; Thess, A.; Smalley, R. E., Evidence for charge transfer in doped carbon nanotube bundles from Raman scattering. *Nature* **1997**, *388*, 257 - 259.
(27) Liu, T.; Xiao, Z.; Wang, B., The exfoliation of SWCNT bundles examined by simultaneous Raman scattering and photoluminescence spectroscopy. *Carbon* **2009**, *47*, 3529-3537.
(28) Yasuda, S.; Hoshina, S.; Chiashi, S.; Maruyama, S.; Murakoshi, K., Electronic structure characterization of an individual single-walled carbon nanotube by in situ electrochemical surface-enhanced Raman scattering spectroscopy. *Nanoscale* **2016**, *8*, 19093-19098.
(29) Kalbac, M.; Kavan, L., Influence of the Resonant Electronic Transition on the Intensity of the Raman Radial Breathing Mode of Single Walled Carbon Nanotubes during Electrochemical Charging. *J. Phys. Chem. C* **2009**, *113*, 16408-16413.
(30) Thomsen, C.; Reich, S.; Rafailov, P. M.; Jantoljak, H., Symmetry of the High-Energy Modes in Carbon Nanotubes. *Phys. Status Solidi B* **1999**, *214*, r15-r16.
(31) Maultzsch, J.; Telg, H.; Reich, S.; Thomsen, C., Radial breathing mode of single-walled carbon nanotubes: Optical transition energies and chiral-index assignment. *Phys. Rev. B* **2005**, *72*, 205438.
(32) Piao, Y.; Simpson, J. R.; Streit, J. K.; Ao, G.; Zheng, M.; Fagan, J. A.; Hight Walker, A. R., Intensity Ratio of Resonant Raman Modes for (n,m) Enriched Semiconducting Carbon Nanotubes. *ACS Nano* **2016**, *10*, 5252-5259.
(33) Popov, V. N.; Henrard, L.; Lambin, P., Resonant Raman Intensity of the Radial Breathing Mode of Single-Walled Carbon Nanotubes within a Nonorthogonal Tight-Binding Model. *Nano Lett.* **2004**, *4*, 1795-1799.
(34) Öberg, S.; Adjizian, J. J.; Erbahar, D.; Rio, J.; Humbert, B.; Dossot, M.; Soldatov, A.; Lefrant, S.; Mevellec, J. Y.; Briddon, P., et al., Effect of functionalization and charging on resonance energy and radial breathing modes of metallic carbon nanotubes. *Phys. Rev. B* **2016**, *93*, 045408.
(35) Rao, A. M.; Chen, J.; Richter, E.; Schlecht, U.; Eklund, P. C.; Haddon, R. C.; Venkateswaran, U. D.; Kwon, Y. K.; Tománek, D., Effect of van der Waals Interactions on the Raman Modes in Single Walled Carbon Nanotubes. *Phys. Rev. Lett.* **2001**, *86*, 3895-3898.
(36) Sun, G.; Kürti, J.; Kertesz, M.; Baughman, R. H., Variations of the Geometries and Band Gaps of Single-Walled Carbon Nanotubes and the Effect of Charge Injection. *J. Phys. Chem. B* **2003**, *107*, 6924-6931.
(37) Preciado-Rivas, M. R.; Torres-Sánchez, V. A.; Mowbray, D. J., Optical Absorption and Energy Loss Spectroscopy of Single-Walled Carbon Nanotubes. **2019**, arXiv:1907.08036.
(38) Gebhardt, J.; Bosch, S.; Hof, F.; Hauke, F.; Hirsch, A.; Görling, A., Selective reduction of SWCNTs – concepts and insights. *J. Mater. Chem. C* **2017**, *5*, 3937-3947.
(39) Chacón-Torres, J. C.; Ganin, A. Y.; Rosseinsky, M. J.; Pichler, T., Raman response of stage-1 graphite intercalation compounds revisited. *Phys. Rev. B* **2012**, *86*, 075406.
(40) Senga, R.; Pichler, T.; Suenaga, K., Electron Spectroscopy of Single Quantum Objects To Directly Correlate the Local Structure to Their Electronic Transport and Optical Properties. *Nano Lett.* **2016**, *16*, 3661-3667.
(41) Mortensen, J. J.; Hansen, L. B.; Jacobsen, K. W., Real-space grid implementation of the projector augmented wave method. *Phys. Rev. B* **2005**, *71*, 035109.
(42) Enkovaara, J.; Rostgaard, C.; Mortensen, J. J.; Chen, J.; Dulak, M.; Ferrighi, L.; Gavnholt, J.; Glinsvad, C.; Haikola, V.; Hansen, H. A., et al., Electronic structure calculations with GPAW: a real-space implementation of the projector augmented-wave method. *J. Phys. Condens. Matter* **2010**, *22*, 253202.
(43) Bahn, S. R.; Jacobsen, K. W., An Object-Oriented Scripting Interface to a Legacy Electronic Structure Code. *Comput. Sci. Eng.* **2002**, *4*, 56-66.
(44) Larsen, A. H.; Mortensen, J. J.; Blomqvist, J.; Castelli, I. E.; Christensen, R.; Dułak, M.; Friis, J.; Groves, M. N.; Hammer, B.; Hargus, C., et al., The atomic simulation environment—a Python library for working with atoms. *J. Phys. Condens. Matter* **2017**, *29*, 273002.
(45) Perdew, J. P.; Zunger, A., Self-interaction correction to density-functional approximations for many-electron systems. *Phys. Rev. B* **1981**, *23*, 5048-5079.
(46) Larsen, A. H.; Vanin, M.; Mortensen, J. J.; Thygesen, K. S.; Jacobsen, K. W., Localized atomic basis set in the projector augmented wave method. *Phys. Rev. B* **2009**, *80*, 195112.
(47) Kramberger, C.; Roth, F.; Schuster, R.; Kraus, R.; Knupfer, M.; Einarsson, E.; Maruyama, S.; Mowbray, D. J.; Rubio, A.; Pichler, T., Channeling of charge carrier plasmons in carbon nanotubes. *Phys. Rev. B* **2012**, *85*, 085424.

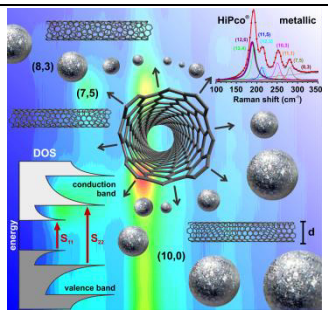
HiPco
metallic
(8,3)
(7,5)
100 150 200 250 300 350
Raman shift (cm⁻¹)
DOS
conduction band
valence band
energy
S_{11}
S_{22}
(10,0)
d

TOC figure